minerals

MDPI

Article

Mineralogical Characterization and Geochemical Signatures of Supergene Kaolinitic Clay Deposits: Insight of Ropp Complex Kaolins, Northcentral Nigeria

Adamu Yunusa [1,2], Hanlie Hong [1,*], Atif Salim [1], Tarig Amam [1], Chen Liu [1], Yanxiao Xu [1], Xiaochao Zuo [3] and Zhaohui Li [4]

[1] School of Earth Sciences, China University of Geosciences, Wuhan 430074, China; adamuyunusageology@gmail.com (A.Y.); xyx@cug.edu.cn (Y.X.)
[2] Department of Geology, Ahmadu Bello University, Zaria 810107, Nigeria
[3] Engineering Research Center of Nano-Geomaterials, Ministry of Education, China University of Geosciences, Wuhan 430074, China; zuoxiaochao@cug.edu.cn
[4] Geoscience Department, University of Wisconsin—Parkside, Kenosha, WI 53144, USA; li@uwp.edu
* Correspondence: honghanlie@cug.edu.cn

Abstract: This study presents the chemical and mineralogical composition of clay deposits and associated rock types within the Ropp Complex in order to assess the influence of parent lithology on the kaolinization, genesis, and utility of the deposit. Representative kaolin samples from E horizons of the weathering profiles and their bedrocks were collected from six sites in the Ropp Complex. Clay mineralogy was determined via the XRD technique, while a geochemical analysis was conducted using XRF, SEM coupled with EDS, and ICP-MS. The results showed that all kaolins dominantly contain kaolinite with a content of 77%–98% except for the AS1 kaolin with only minor kaolinite (20%) but mainly illite (65%). The notably lower crystallinity of kaolinite (HI value of 0.53–1.1) as well as its markedly small grain size is consistent with the formation of kaolinite from intensive chemical weathering of igneous rocks. The AS1 kaolin was probably formed from hydrothermal alteration in the burial stage due to the heating of groundwater by the late volcanism. Mobile trace elements (Sr, Ba, and Eu) exhibited a depletion trend, while immobile elements (Hf, Ta, Th) showed enrichment. The relatively more zirconium in kaolins implies the formation of low-temperature kaolinization. The notably high kaolinite content, accompanied by reasonable levels of Fe_2O_3 and TiO_2, signifies a medium-grade quality. Furthermore, chondrite-normalized rare earth element (REE) patterns exhibit congruent trends in rocks and kaolin samples, indicating a relative enrichment in light rare earth elements (LREEs) alongside a discernible negative Eu anomaly. The abundant kaolinite and silicon–aluminum composition make the kaolins suitable for refractories, pharmaceutics, cosmetics, and supplementary cementitious material (SCM).

Keywords: Ropp complex; kaolinite deposit; genesis; weathering; clay minerals

Citation: Yunusa, A.; Hong, H.; Salim, A.; Amam, T.; Liu, C.; Xu, Y.; Zuo, X.; Li, Z. Mineralogical Characterization and Geochemical Signatures of Supergene Kaolinitic Clay Deposits: Insight of Ropp Complex Kaolins, Northcentral Nigeria. *Minerals* **2024**, *14*, 869. https://doi.org/10.3390/min14090869

Academic Editor: Manuel Pozo Rodríguez

Received: 15 July 2024
Revised: 20 August 2024
Accepted: 21 August 2024
Published: 27 August 2024

1. Introduction

Industrial minerals and clays are pivotal components within various industrial sectors [1–3]. Consequently, exploring and assessing these resources hold critical significance for emerging economies. The kaolinite group minerals ($Al_2Si_2O_5(OH)_4$) are derived from the chemical weathering of aluminum-rich silicate minerals in different types of rocks and soils [4–6]. This group comprises kaolinite, dickite, halloysite, and nacrite, each characterized by unique structural arrangements [7].

Kaolinite group minerals find extensive utility in diverse industrial applications, contributing significantly to many nations' economic and technological development [8]. Global demand for kaolin continues to rise [9]. To meet local and international needs, it is

imperative to accurately assess and characterize the nation's kaolin deposits, which offer potential economic benefits in terms of GDP and foreign exchange earnings.

While kaolin suitable for industrial use is relatively scarce worldwide, notable deposits exist in the Cornwall and Devon regions of southwest England and along the Jari and Capim Rivers in the northern region of Brazil, specifically the Amazon, which are acknowledged as the world's largest and best quality primary kaolin deposits [10]. However, such kaolin is widely spread all over the world (Turkey, India, Russia, Iran, China, and so on). In Africa, prominent kaolin occurrences are primarily found in Nigeria, Uganda, Egypt, Eritrea, and South Africa [11]. Nigeria, in particular, boasts substantial reserves of primary and secondary kaolin [9,12], with numerous deposits identified, especially in regions supported by the younger granites and sedimentary basins [13], amounting to approximately three billion metric tons, as stated by the Raw Material Research Council of Nigeria [14]. Over forty kaolin deposits were identified in Nigeria [9]. To stimulate domestic sector growth, Nigeria has imposed a ban on kaolin imports [14,15].

The genesis of kaolin deposits in Nigeria predominantly arises from the intricate interplay of geological processes, chiefly encompassing the phenomena of weathering and hydrothermal alteration acting upon the parent rocks [16]. In the Nigerian context, supergene kaolin deposits commonly form in areas characterized by tropical climatic conditions distinguished by abundant rainfall, fostering an environment conducive to profound weathering and leaching mechanisms [9]. The alteration of rock-forming minerals, such as feldspar and muscovite, in igneous bedrocks into kaolin is predominantly influenced by variables, including the chemical composition of the parent rock and the prevailing climatic and hydrological conditions within the supergene environment [17].

Numerous research endeavors have explored the widespread Nigerian clay deposits and have been thoroughly examined for various applications (Ref. [16], and references therein). Daspan et al. (2009) conducted an initial physical as well as chemical evaluation of Kuba kaolin deposits to study its industrial potential, and their findings revealed that the clay is medium grade and appropriate for use in manufacturing paper, paint, and ceramics [18]. Christopher et al. (2013) further investigated the Kuba clays and discovered that they have a low kaolinite concentration but a reasonably high montmorillonite content [19]. Odewumi et al. (2015) investigated the Kuba and Nahuta clays and concluded that Nahuta clays formed from the chemical weathering of felsic rock, and Kuba clays were derived from the weathering of mixed sources (felsic and mafic rocks) [20]. Geochemical characteristics and their implications for the paleo weathering proxy of soil profiles in Nahuta clays were also undertaken in a recent study [21].

Although a number of studies on clay deposits in Nigeria have been undertaken, a rare investigation was performed on clay deposits of the Ropp Complex. Oyawoye and Hirst (1964) reported the presence of montmorillonite in the Ropp Complex's younger granites of Nigeria [22], whereas the mineral characteristics and formation of the clay deposits remain largely unknown. Moreover, the mineralogical and geochemical properties of clays in the clay ore deposit are essential for their quality and possible industrial uses [23]. In this study, we explore the genesis, mineralogical diversity, and geochemical signatures of kaolinitic clays within the complex. Through a detailed analysis of kaolinitic saprolites and their bedrock across various locations, we offer unprecedented insights into the formation and mineralogy of kaolin, enriching our understanding of the geological history. Our investigation focuses specifically on the saprolite horizon, which typically has the highest kaolinite content within the profile. We did not conduct a comprehensive examination of the entire profile, as commonly performed in typical regolith studies, with aims to (1) analyze the hidden lateral variations and potential source influences on studying multiple kaolin deposits within the Ropp Complex and (2) obtain a more comprehensive understanding of the formation of the kaolinite deposits.

2. Geological Settings

The Ropp Complex (Figure 1) is located in the northeastern part of Plateau State, bordered by the Barikin Ladi, Bokkos, and Mangu Local Government Area. This region forms a roughly triangular area of about 622 km^2, with approximately 183 km^2 underlain by units of alkaline granite [24]. The Complex is notable for its mineralization and contains economically valuable minerals, such as tin and columbite [25].

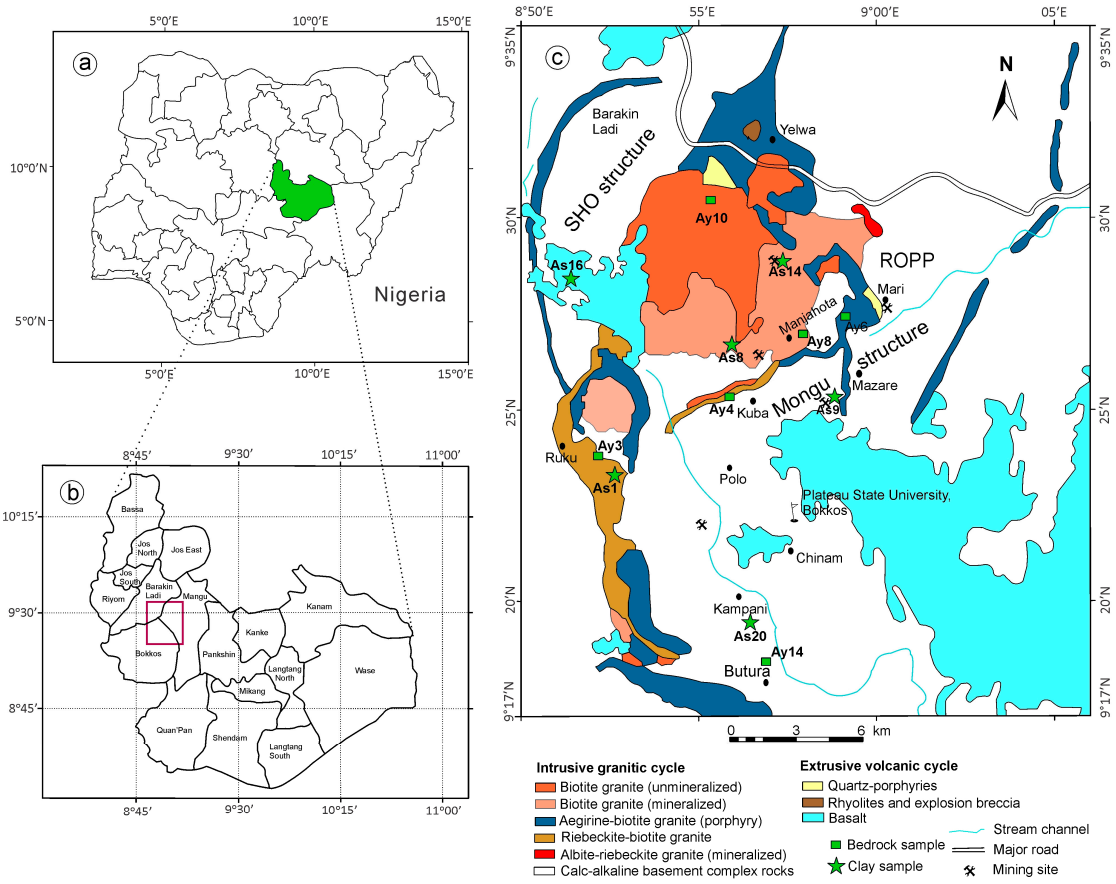

Figure 1. A geologic map of the study area (modified from [26]). (**a**,**b**) generalized maps showing the location (the purple square) of the Ropp Complex, (**c**) a geological map showing lithology of the study area and sampling sites.

Encircling the Ropp Complex is an arcuate and polygonal ring dyke that encompasses a basement and a prominent central massif of rugged younger granite hills [27]. Some of these central hills rise over 300 m above the plateau, creating prominent landmarks. The Ropp Complex features distinct volcanic and plutonic cycles. The granitic intrusion cycle began with coarse-grained granite porphyry, akin to the Jos-Bukuru Complex, followed by a series of biotite and riebeckite granites. Later stages included recurring granite porphyry, hornblende–biotite granite, and late biotite granites. The volcanic cycle comprises quartz porphyries, rhyolites and explosion breccias, and early basic dykes [24].

The Ropp Complex predominantly consists of biotite granite along with minor albite arfvedsonite granites, which occasionally show rare metal Nb-Sn mineralization [24,28]. The biotite granite in Bukka Bakwai village holds the highest primary columbite, while the Ropp biotite granites rank second in tin production after the Jos-Bukuru biotite granites [24,29]. The Ropp alkaline A-type granites have coeval intrusive ages ranging from 161.1 ± 1.7 Ma to 162.3 ± 5.1 Ma, with chemical characteristics indicative of alkaline ferroan granites [26].

The Ropp Complex is known to be deformed by shearing, faulting, and jointing [27]. The study area features a massive, elongated intrusion of riebeckite–biotite granite porphyry. This intrusion includes a small, flat-lying sheet in the core of the complex, positioned

above the older biotite granite. In the southwest, this structure appears as an eroded dome bordered by a small ring dyke, creating an elongated crescent. A notable crescentic intrusion of granite porphyry extends 9.6 km at the complex's northern end, with a maximum width of 2.3 km.

The biotite granite is mainly found at the center of the Complex. Some of the granites, especially in Gana, are compositionally similar to the N'gell biotite granite of the Jos-Bukuru complex and exhibit lower columbite concentrations and less evidence of tin mineralization [24]. Beneath the aegirine biotite granite, multiple screens indicate its more extensive spread. The central massif is characterized by rugged boulder-strewn hills rising hundreds of meters above the surrounding lowlands. The southern core of the complex comprises the biotite granite of the Bukka Bakwai hamlet, flanked by the aegirine biotite granite. The albite arfvedsonite granite, which is greyish and coarse-grained to porphyritic, shows noticeable acicular grains of sodic amphiboles and clear replacement textures [28]. The Bukka Bakwai biotite granite contains the biggest primary columbite deposits in the Ropp Complex [24,29].

3. Samples and Methods

3.1. Sampling

The study area exhibits a unique occurrence of kaolin deposits formed through supergene processes associated with weathering tin-bearing minerals within the rocks. The deposits are found beneath the tin-bearing bedrock where active tin mining operations are ongoing. The weathering of tin-bearing minerals and other rock components is believed to be the primary process responsible for the supergene kaolin formation. Robust placer mining operations were also observed, which focused on extracting tin from alluvial deposits along the intricate network of river channels. Road banks and hillside exposures contribute to the exposure of kaolin deposits in the area, providing convenient access for sample collection (Figure 2a,b). Notably, tailings from mining pits are found to be kaolinized and left as hilly dumps. An intriguing feature observed was the presence of three distinct horizons, particularly near Manjahota and Kuba, with laterite cappings (Figure 2c).

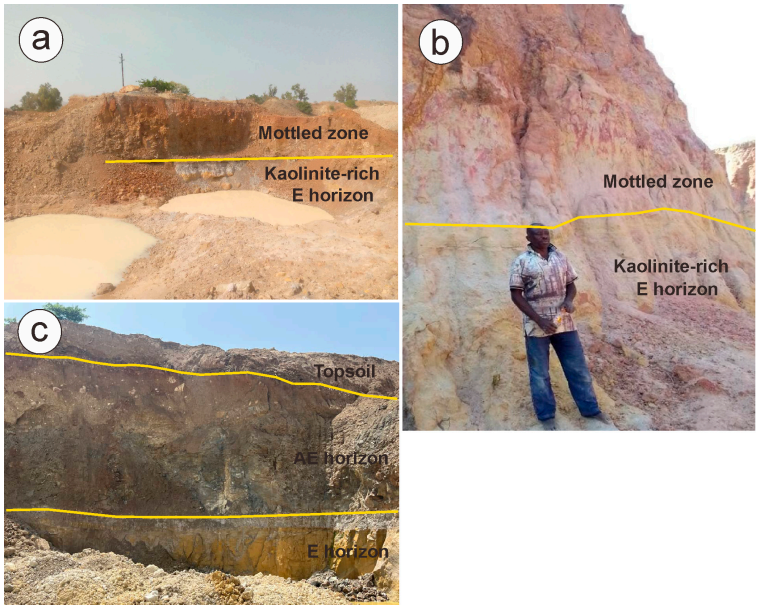

Figure 2. Field images showing two distinct occurrences of kaolin in the weathering profiles of the Ropp Complex. (**a**) The overview of white kaolinite, (**b**) the close-up view of white kaolinite, and (**c**) yellow kaolinite in the E horizon.

Samples were collected from the illuvial horizon of the weathering profiles as well as the relevant bedrocks. The illuvial horizon often displays variations in height and thickness

across different occurrences. About 400 g of each of the twenty raw clay samples were taken at different locations within the Ropp Complex. The representative samples collected were stored in sample bags to prevent any potential contamination. The samples were air-dried for two weeks and then crushed manually to powder at 0.07 mm in size for geochemical and mineralogical analyses. Preliminary XRD investigations of the samples showed that mineral compositions in most of samples above with the same parent bedrock were relatively uniform, and twenty kaolin samples were divided into six kinds of representative samples according to their distinct color and associated accessory mineral components. In further measurement, six representative kaolin and rock samples were selected for further geochemical and mineralogical analyses, respectively.

3.2. Methods

XRD was used to characterize the mineralogical composition of the samples, while SEM/EDS was employed to analyze the morphology and chemical composition of each mineral, respectively.

The XRD measurement was performed on a Panalytical X'Pert PRO DY2198 (PANalytical Co., Ltd., Eindhoven, The Netherlands) at the State Key Laboratory of Biogeology and Environmental Geology of the China University of Geosciences, Wuhan, China. The whole-rock sample was used to determine the mineral composition, and the clay fraction (<2 mm) obtained by the sedimentation method was used for the clay mineralogical investigation. The whole-rock powder samples were prepared by mounting the powders into sample holders using a back-press technique. The oriented clay-fraction samples were prepared by the following procedures. Carbonate minerals were removed from the samples by treating them with 10 mL of HCl acid. To remove organic matter, approximately 5 mL of hydrogen peroxide was added to the sample. A total of 400 mL of water was mixed in a quantity of sodium hexametaphosphate and was then incorporated into the mixture. The entire solution was stirred using a kitchen-type rotary mixer to facilitate the gravity settling of clays to obtain the <2 μm fraction. The mixture was placed into centrifuge tubes and centrifuged at 1000 rpm for two minutes to concentrate the clay fraction. The upper 2 cm of the suspension were selected and centrifuged at 3000 rpm for eight minutes. Finally, the concentrated clay fraction was placed onto a glass slide and allowed to dry at room temperature. Each clay-fraction sample was analyzed after being air-dried and undergoing ethylene glycol solvation in a sealed glass container at 60 °C for about eight hours.

Minerals were identified by characteristic reflections [30]. Non-clay minerals were identified using the following reflections: quartz, 4.26 Å and 3.34 Å; orthoclase, 3.24 Å; and ettringite, 9.92 Å and 3.85 Å, respectively. The mineral contents of the whole-rock samples were estimated using the reference intensity ratio approach with admixture of corundum as the internal standard [31]. The basal 001 reflection of air-dried and glycolated smectite is ~15 Å and 17 Å, and the 001 and 002 reflections of kaolinite are 7.16 Å and 3.57 Å, respectively. Illite was identified using the 10 Å, 5 Å, and 3.34 Å reflections. The 'crystallinity' (degree of structural order) of kaolinite was measured using the Hinckley index, which was calculated as the rate of the sum of (1$\bar{1}$0) and (11$\bar{1}$) heights from above a line drawn from the trough between the (020)–(1$\bar{1}$0) peaks to the total height above background of the (1$\bar{1}$0) reflection [32].

For SEM-EDS analysis, a small number of sample fragments were prepared by gold-coating and analyzed at the SEM laboratory of the School of Materials Science and Chemistry, China University of Geosciences, Wuhan, China, using Hitachi SU8010 Ultra High-Resolution Scanning Electron Microscope (Hitachi Ltd., Tokyo, Japan) equipped with an energy dispersive X-ray spectroscopy detector for elemental analysis.

The geochemical analysis of kaolin samples and their host rock samples was performed using X-ray Fluorescence (XRF) and Inductively Coupled Plasma Mass Spectrometry (ICP-MS) at Wuhan Sample Solution Analytical Technology Co., Ltd., Wuhan, China. The sample pretreatment for major rock element analysis involved the melting method, using a flux mixture of lithium tetraborate, lithium metaborate, and lithium fluoride

(45:10:5). Ammonium nitrate and lithium bromide were used as oxidants and release agents, respectively. The melting temperature was set at 1050 °C for 15 min. Major element analysis was conducted using a RIGAKU XRF spectrometer (Rigaku Corporation, Japan) with a 4.0 kW end window and an Rh target. The test conditions included a voltage of 50 kV and a current of 60 mA. Trace element analysis was conducted using an Agilent 7700e ICP-MS (Agilent Technologies, Inc., Santa Clara, CA, USA). Sample powder was dried, weighed, and dissolved in a Teflon bomb with nitric and hydrofluoric acids. The solution was heated, evaporated, and treated further. Finally, the solution was transferred to a polyethylene bottle and diluted for analysis.

The chemical index of weathering (CIW), index of compositional variability (ICV), and chemical index of alteration (CIA) for each sample were calculated by employing the following equations [33–35]:

$$CIW = \{Al_2O_3/(Al_2O_3 + CaO + Na_2O)\} \times 100$$

$$CIA = \{Al_2O_3/(Al_2O_3 + CaO + Na_2O + K_2O)\} \times 100$$

$$ICV = \{CaO + K_2O + Na_2O + Fe_2O_3(t) + MgO + MnO + TiO_2\}/Al_2O_3$$

4. Results

4.1. Mineralogy of the Kaolin Deposits

The mineral components in the Ropp Complex whole-rock kaolin samples are dominantly kaolinite, with only minor amounts of smectite, quartz, orthoclase, and ettringite (Figure 3a). Mineral abundances displayed only small changes between samples from the same bedrock but varied significantly between samples derived from different bedrocks, as reflected by intensities of their characteristic peaks of the minerals (Figure 3a). Kaolinite is identified by the presence of basal diffraction near 7 Å in the air-dried sample, which remain stable after the ethylene–glycol solvation, and the presence of smectite is indicated by the 15 Å peak in the air-dried sample, which expands to 17 Å after glycolated treatment (Figure 3b). Sample AS1 consists dominantly of illite and kaolinite, with minor amounts of smectite and quartz. Samples AS8, AS14, and AS16 have the same mineral assemblage of mainly kaolinite and quartz, while the content of quartz shows a decreasing trend. The AS9 sample contains mainly kaolinite, with minor amounts of smectite, quartz, and orthoclase. The AS20 sample consists of mainly kaolinite with minor quartz, ettringite, and hematite. The percentage of each mineral in the Ropp Complex kaolin samples is summarized in Table 1. Except for the presence of a large proportion of illite in sample AS1, all other samples dominantly contain kaolinite with a proportion of 77%–98%, indicating the kaolinite ore samples are notably pure with only minimal contamination from other minerals or impurities. Kaolinite in samples AS20 and AS1 have relatively higher HI values of 1.1 and 1.0, while the kaolinite of samples AS8, AS9, AS14, and AS16 have significantly lower HI values of 0.80, 0.65, 0.73, and 0.53, respectively (Table 1), consistent with kaolinite formed from the supergene weathering of igneous rocks [36].

Table 1. Mineral compositions of whole-rock samples from the Ropp Complex clay deposits (wt%).

Sample	AS1	AS8	AS9	AS14	AS16	AS20
Color	**Grayish Yellow**	**Light Grey**	**Dark Grey**	**Grey White**	**Light Pink**	**Yellow**
kaolinite	20	79	77	94	98	84
illite	65	/	/	/	/	/
smectite	9	5	12	/	/	/
quartz	6	16	8	6	2	7
orthoclase	/	/	3	/	/	/
ettringite	/	/	/	/	/	5
hematite	/	/	/	/	/	4
HI	1.0	0.80	0.65	0.73	0.53	1.1

"/": under detection limit.

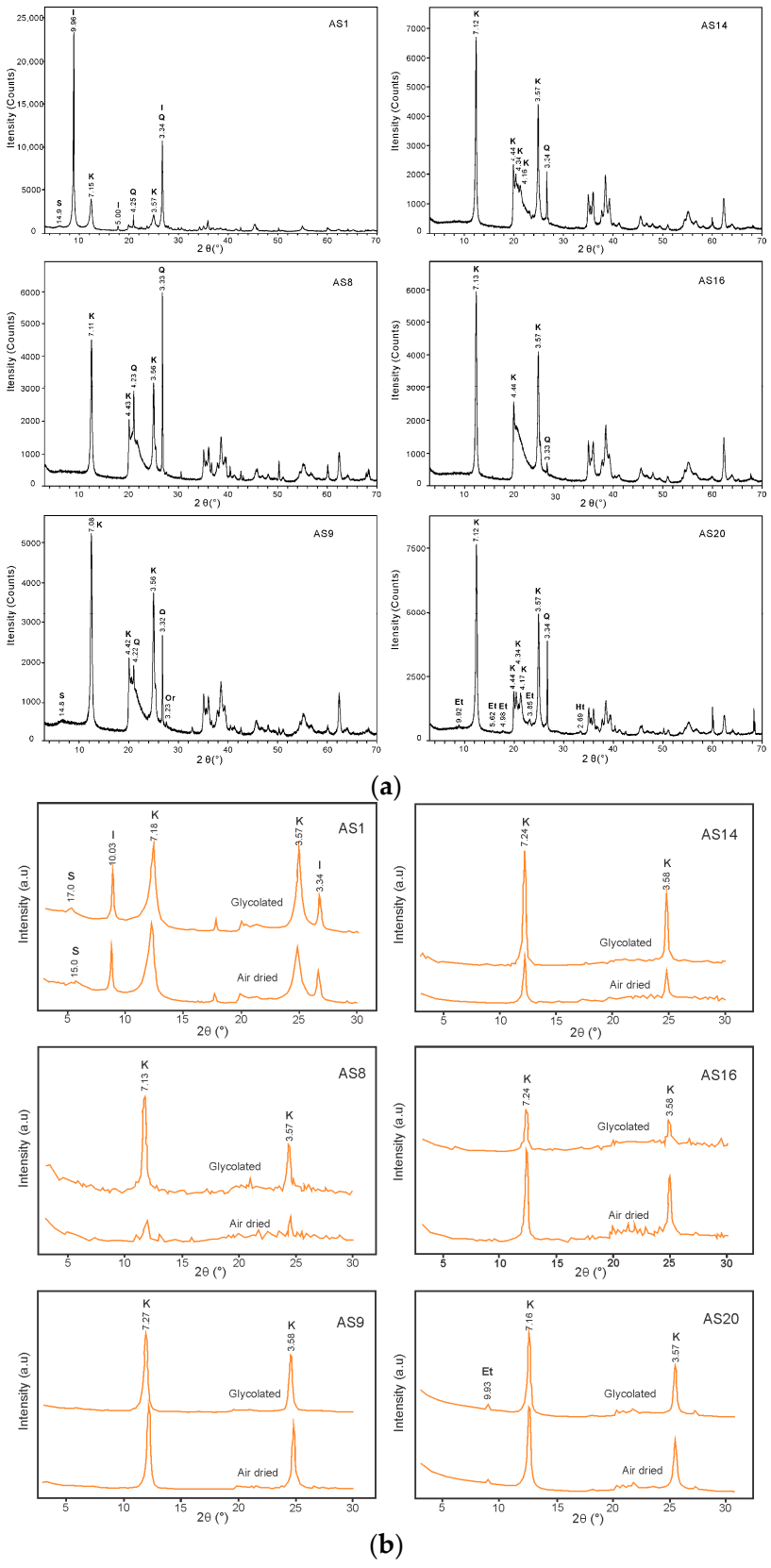

Figure 3. (**a**) XRD patterns of representative whole-rock samples of the Ropp Complex kaolinite deposits. I: illite; S: smectite; K: kaolinite; Q: quartz; Or: orthoclase; Et: ettringite; Ht: hematite. (**b**) XRD patterns of the samples showing the presence of kaolinite (K), smectite (S), and illite (I); Et: ettringite.

4.2. SEM-EDS Analysis

Detailed scanning electron micrographs coupled with EDS spectra show significant differences between the samples from different locations. In general, kaolinite was characterized by its layered structure and appears as thinly platy crystals with a smooth basal surface. However, kaolinite in different samples displayed marked difference in its grain size and edge surface and thus showed clearly different morphological characteristics between the six kaolin-ore samples. Sample AS1 contains kaolinite with relatively large grain size and aggregates of small rectangular illite in pore space (Figure 4a). Kaolinite sample AS14 exhibits euhedral pseudo-hexagonal morphology, characteristic of kaolinite minerals (Figure 4b). Also, in sample AS20, kaolinite exhibits characteristic book-like aggregates of pseudo-hexagonal crystals (Figure 4c). The well-developed euhedral pseudo-hexagonal crystals usually have large grain sizes, ranging from 0.5 to 5.0 μm. Most of kaolinite crystals in samples AS8, AS9, and AS16 occur in poorly developed thin plates with a relatively smooth or flat basal (001) plane, but their lateral surfaces (110) and (010) were poorly developed and extremely small and thus exhibit irregularly ragged outlines (Figure 4d–f). The particle sizes are quite uniform and usually small, ranging generally from 0.3 to 0.6 μm. The spectra from the EDS in all the samples show that kaolinite is primarily composed of silicon, aluminum, and oxygen in significant amounts. The presence of Fe, Mg, Ti, and Ba in the kaolinite indicates the presence of impurities. EDS spectra for illite indicate the presence of potassium in addition to silicon, aluminum, and oxygen. The presence of potassium in the illite is notable and helps distinguish it from kaolinite.

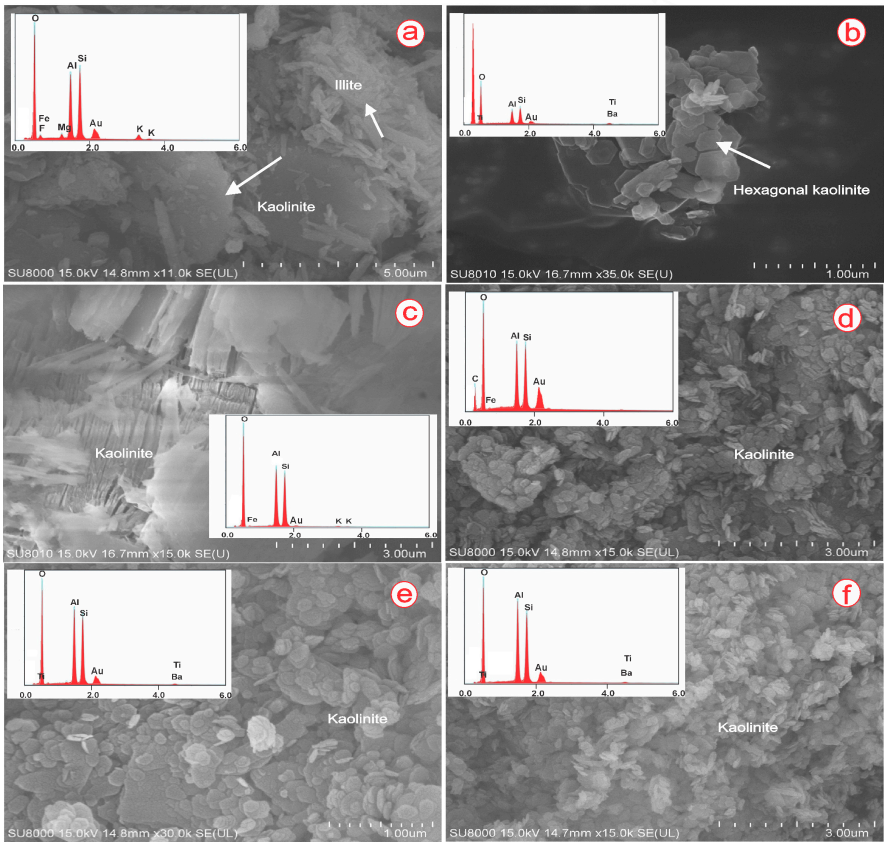

Figure 4. Scanning electron micrographs with corresponding EDS spectra illustrating the morphology and chemical composition of kaolinite and associated minerals. (**a**) Aggregates of small elongated-plate illite in pore space showing precipitation from the solution, kaolinite occurring in relatively large plates (AS1). (**b**) Hexagonal kaolinite plates from sample AS14. (**c**) The characteristic book-like aggregates of kaolinite (AS20). (**d–f**) Kaolinite flakes with irregular outlines (AS8, AS9, and AS16).

4.3. Major Geochemical Composition and Degree of Weathering

The distribution of major elements indicates the origin and suitability of clays for industrial purposes [37–39]. The SiO_2 content of the bedrocks ranges from 77.80 to 55.71%, with a mean value of 70.32%, consistent with their acidic lithology (Table 2).

Table 2. Major oxide compositions of whole-rock clays (AS) and the relative bedrocks (AY) (wt%).

Samples	Rock Type	SiO_2	TiO_2	Al_2O_3	Fe_2O_3	MnO	MgO	CaO	Na_2O	K_2O	P_2O_5	LOI	SUM
AS1	RBG	52.62	0.95	23.19	7.54	0.07	2.55	0.34	0.42	4.34	0.18	7.02	99.22
AS8	BGM	53.77	2.01	29.83	1.69	0.01	0.09	0.15	0.01	0.10	0.05	11.80	99.51
AS9	CAB	44.25	2.75	32.46	2.97	0.02	0.14	0.19	0.03	0.13	0.07	16.73	99.73
AS14	BGM	47.26	1.14	35.86	1.73	0.01	0.03	0.07	0.01	0.08	0.05	13.22	99.47
AS16	B	47.63	1.73	35.87	1.23	0.01	0.02	0.06	0.00	0.03	0.06	13.11	99.75
AS20	CAB	51.88	0.64	30.95	4.04	0.02	0.08	0.09	0.02	0.26	0.13	11.58	99.68
AY3	RBG	76.02	0.04	12.98	1.18	0.02	0.05	0.33	4.28	4.45	0.01	0.46	99.81
AY4	RBG	69.05	0.57	14.92	3.61	0.06	0.82	2.23	4.31	3.64	0.15	0.55	99.91
AY6	ABG	77.80	0.12	11.91	1.03	0.00	0.05	0.07	3.68	4.86	0.00	0.41	99.93
AY8	BGM	67.82	0.28	16.23	2.53	0.05	0.81	1.76	3.50	5.80	0.37	0.78	99.93
AY10	BGU	75.53	0.06	12.91	1.17	0.02	0.04	0.48	4.00	4.78	0.00	0.38	99.38
AY14	CAB	55.71	0.92	15.94	8.50	0.15	4.79	6.87	3.43	2.15	0.28	0.61	99.36

RBG: Riebeckite–biotite granite; ABG: aegirine biotite granite; BGM: biotite granite (mineralized); BGU: biotite granite (unmineralized); CAB: calc-alkaline basement complex; B: basalt; LOI: loss on ignition.

The kaolin deposits of the study area have significant quantities of SiO_2 (44.25%–52.62%) and Fe_2O_3 (1.23%–7.54%). Samples AS14 and AS16 show compositions similar to that of pure kaolinite (46.30% SiO_2 and 39.80% Al_2O_3) [40], consistent with their mineral compositions that are overwhelmingly kaolinite. The Fe_2O_3 content of the deposits is higher than the permissible limits for kaolin in industrial uses (1%) [41], even though it depends on the industry. This concentration of Fe_2O_3 present in the deposits is likely attributed to the alteration of iron-bearing minerals within the bedrock. However, for certain types of ceramics, such as stoneware or earthenware, which have a more rustic or natural aesthetic, slightly higher concentrations of iron oxide may be acceptable. In this case, an iron oxide level of up to 2% can contribute to color variations, improving the appearance of the final product. The deposits are characterized by appreciable concentrations of Al_2O_3 (23.19–35.87%), which are lower than the commercial-grade ceramic value (37%–38%) [41]. The concentrations of mobile element oxides in the deposits are modest when compared to Fe_2O_3 {CaO (0.06%–0.34 wt%), MgO (0.02%–2.55%), P_2O_5 (0.05%–0.18%), and MnO (0.01%–0.07%)}, which indicates a total loss of these mobile elements during the process of kaolinization.

Sample AS1 contains markedly more K_2O (4.34%), Na_2O (0.42%), MgO (2.55%), CaO (0.34%), and Fe_2O_3 (7.54%) compared to the other kaolin-ore samples due to the presence of large amounts of illite. Conversely, other kaolin-ore samples have significantly low levels of CaO, MgO, K_2O, and Na_2O contents, pointing to the low level of impurities. The TiO_2 value varies from 0.638 to 2.75%

With an average of 1.53%, all additional elements, including iron, have been mobilized with the exception of aluminum and titanium, which remain relatively immobile.

Figure 5 illustrates the correlation between Al_2O_3 and each of the following, SiO_2, Fe_2O_3, K_2O, Na_2O, and CaO, showing a positive correlation between Al_2O_3 and TiO_2, indicating the presence of titanium-bearing minerals. The negative correlations between Al_2O_3 and SiO_2, Fe_2O_3, and CaO indicate the depletion or removal of silicate, iron, and calcium minerals during the alteration process. The observed positive correlation between Al_2O_3 and TiO_2 indicates that these elements were relatively immobile during weathering, while the negative correlation observed between Al_2O_3 and SiO_2 as well as that of CaO suggests the preferential leaching of Si and Ca during weathering, potentially due to feldspar breakdown.

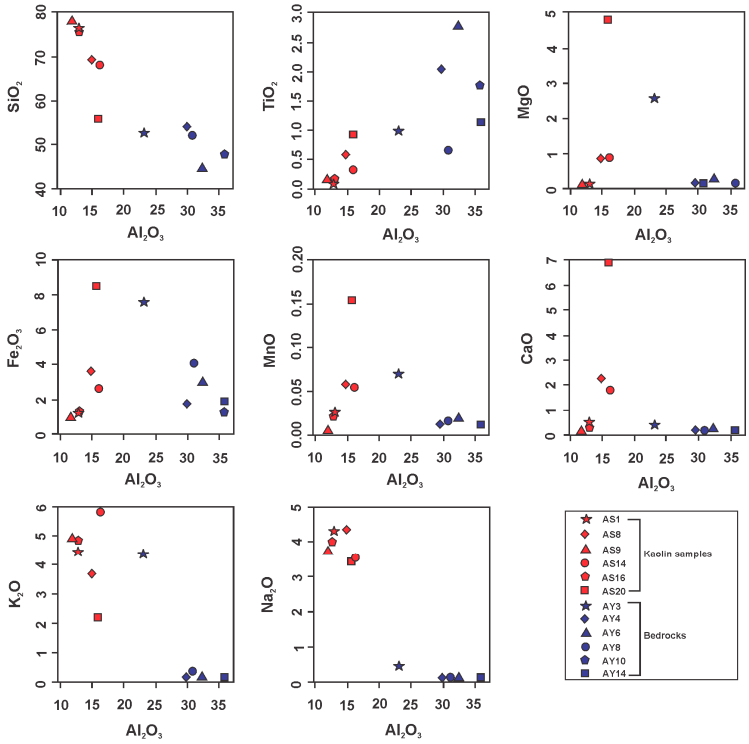

Figure 5. Harker diagram showing the relation between Al_2O_3 and other oxides.

The CIW, ICV, and CIA for each sample (Figure 6a,b) were contrasted with well-known kaolins. The CIA and CIW of any deposit can be used to identify the degree to which potassium feldspar and micas have been transformed into clay minerals [42]. Any kaolin deposit with a high CIW and CIA value (>80) indicates an exceptionally high level of silicate weathering and therefore shows the deposit's maturity [43]. In this work, the clay samples are plotted within the field of 'Extreme Silicate Weathering', which confirms the advanced degree of weathering. The ICV is used to compare the abundance of Al_2O_3 to the other major oxides found in kaolins.

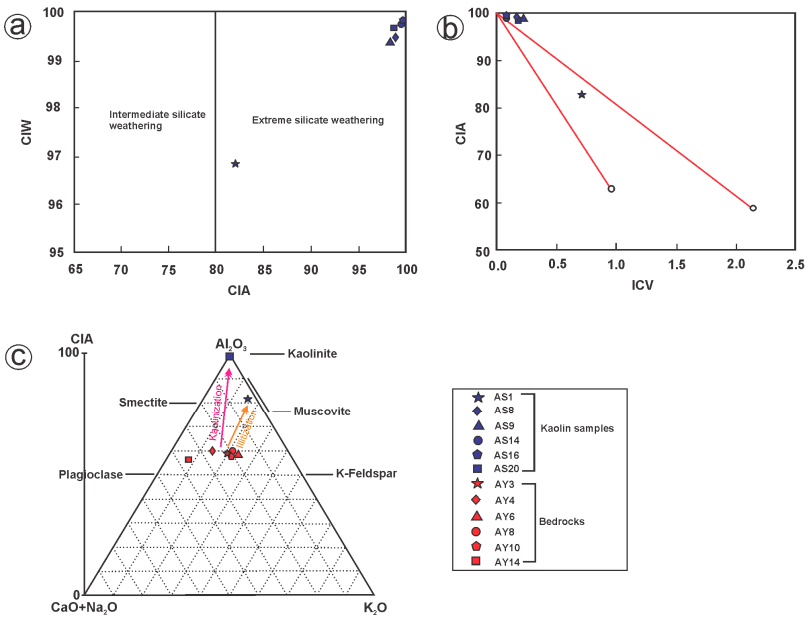

Figure 6. The relation between CIW and CIA (**a**), CIA and ICV (**b**), and the ACNK diagram in molecular proportions (**c**) for the clay samples.

The ternary diagram $Al_2O_3{}^{-}$(CaO + Na_2O)-K_2O (A-CN-K) diagram is employed to determine the weathering trend [34,44–46]. All of the kaolin samples show an intensive weathering history on the ACNK diagram and cluster towards Al_2O_3 (Figure 6c).

The kaolin samples had SiO_2/Al_2O_3 ratios ranging from 1.32 to 2.27 (Table 3), which is more than the stoichiometric SiO_2/Al_2O_3 ratio (1.18) [40]. Sample AS1 has the greatest SiO_2/Al_2O_3 ratio (2.27). The ICV of the examined kaolins varies between 0.09 (AS14 and AS16) and 0.70 (AS1). The elemental composition of the kaolin is compared with industrial specifications (Table 4). The composition is quite consistent with the renowned standard kaolin found in the Cornwell deposits, Sekeharman kaolin (SKD). The high SiO_2, LOI, and Al_2O_3 values in the analyzed kaolin match favorably with pharmaceutical, ceramic, porcelain, paper coating, and refractory brick standards.

Table 3. Elemental ratios and weathering indices of the Ropp Complex kaolins.

Samples	Rock Type	SiO_2/Al_2O_3	CIW	CIA	ICV
AS1	RBG	2.27	96.82	81.96	0.70
AS8	BGM	1.80	99.46	99.14	0.14
AS9	CAB	1.36	99.34	98.95	0.19
AS14	BGM	1.32	99.77	99.56	0.09
AS16	BST	1.33	99.83	99.73	0.09
AS20	CAB	1.68	99.66	98.82	0.17

Table 4. The comparative chemical composition of the kaolin deposits against established standards and specifications (wt%) [37,47–52].

Samples	SiO_2	TiO_2	Al_2O_3	Fe_2O_3	MgO	CaO	Na_2O	K_2O	LOI
Ropp	49.57	1.54	31.36	3.20	0.49	0.15	0.08	0.82	12.24
ECC	47.00	0.03	38.00	0.39	0.10	0.03	0.15	0.80	13.00
SKD	50.00	1.00	32.90	1.20	0.30	0.20	0.20	1.60	12.60
Pharmaceuticals	48.00	0.02	36.00	0.10	0.20	0.01	0.10	1.10	11.90
Ceramics	48.00	0.30	37.00	0.60	0.30	0.10	0.10	1.60	12.40
Filling agent	48.70	0.05	36.00	0.82	0.25	0.60	0.10	2.10	11.90
Fertilizer	46.07	0.50	38.07	0.33	0.01	0.38	0.27	0.43	13.47
Porcelain	48.00	0.03	37.00	0.60	0.30	0.10	0.10	1.60	12.40
Refractory bricks	51–70	1.00–2.80	25–44	0.50–2.40	0.20–0.70	0.10–0.20	0.80–3.50	-	-

4.4. Trace Element Concentration

Kaolin deposits, except sample AS1, have greater concentrations of a set of trace elements, including Hf, Pb, Th, Nb, Ga, Cr, Ni, Ta, and U (Table 5). Zr shows an increase in all the studied kaolin samples, reaching up to 872 ppm, while depletion, especially for Cs and Rb as compared to the parent rock, was also observed. High values of chromophore elements (V, Cr, and Cu) were also noted in the kaolins as compared to the parent rocks. The binary plot of Ba + Sr versus Ce + Y+La, TiO_2 versus Zr, Cr + Nb versus TiO_2 + Fe_2O_3, and ternary plot of Pb, Ba + Sr and Ce + Y+La have been widely used to distinguish hypogene and supergene kaolin formation [53]. All the Ropp Complex kaolinites were plotted within the field of supergene origin on both the binary and ternary diagram except sample AS1 in the field of hypogene origin (Figure 7a,b).

Table 5. Trace element concentrations of whole-rock clays (AS) and the relative bedrocks (AY) (ppm).

Samples	AS1	AS8	AS9	AS14	AS16	AS20	AY3	AY4	AY6	AY8	AY10	AY14
Rock Type	RBG	BGM	CAB	BGM	BST	CAB	RBG	RBG	ABG	BGM	BGU	CAB
Sr	122	62.8	68.1	40.2	48.7	79.6	3.6	204	2.5	245	6.3	513
Zr	284	666	463	872	784	579	127	368	507	99.5	154	60.3
Nb	18.6	245	80.2	239	74.8	32.9	140	21.8	134	8.9	187	11.5

Table 5. *Cont.*

Samples	AS1	AS8	AS9	AS14	AS16	AS20	AY3	AY4	AY6	AY8	AY10	AY14
Rock Type	**RBG**	**BGM**	**CAB**	**BGM**	**BST**	**CAB**	**RBG**	**RBG**	**ABG**	**BGM**	**BGU**	**CAB**
Sn	177	43.9	10.5	46.0	65.5	26.1	8.4	21.2	10.9	4.7	12.2	3.6
Cs	27.5	2.1	1.7	1.6	0.07	0.9	6.2	7.7	2.5	14.6	8.8	14.2
Ba	911	109	109	34.6	82.4	109	7.4	437	14.1	1646	20.9	386
Hf	7.5	25.3	12.0	57.8	23.3	16.8	11.4	10.3	18.5	2.8	9.0	2.0
Ta	1.0	40.0	4.9	32.9	6.0	6.3	37.4	1.8	10.1	1.1	24.8	0.8
Tl	5.0	0.3	0.8	0.2	0.0	0.2	2.9	1.7	1.1	1.0	2.3	0.7
Pb	48.9	96.1	30.2	70.8	60.6	88.6	33.6	39.6	20.2	45.8	30.3	19.3
Th	9.3	46.2	24.6	62.8	34.3	24.9	48.5	55.5	26.6	1.8	44.0	4.7
U	3.2	14.5	4.9	13.6	3.6	4.6	5.7	7.0	5.9	1.6	12.7	2.2
Sc	17.1	11.4	29.2	8.8	14.9	9.4	1.1	5.0	0.5	5.1	1.2	24.0
Co	15.1	2.2	7.3	1.6	2.1	7.7	0.1	6.7	0.4	5.3	0.2	26.1
Li	239	27.0	75.7	17.4	14.1	17.6	371	20.8	33.7	36.8	169	68.1
Be	130	10.3	4.5	3.1	1.7	5.2	8.3	16.6	5.5	5.6	9.5	3.6
V	96.5	63.2	208	41.0	63.4	84.5	1.1	34.1	1.1	36.6	1.0	194
Cr	60.1	63.0	223	65.8	70.4	75.0	0.7	9.8	1.1	6.2	0.8	87.7
Ni	17.0	18.3	47.5	19.7	28.8	19.3	0.3	5.4	0.4	4.9	0.2	33.3
Cu	124	43.4	83.8	21.9	15.0	25.3	0.6	11.9	2.2	3.2	1.0	23.4
Zn	1540	115	97.3	108	59.1	58.2	81.6	175	85.9	51.2	50.1	104
Ga	36.4	87.7	54.7	122	54.8	50.4	63.8	30.5	48.5	20.7	47.7	21.9
Rb	674	11.9	8.9	27.8	0.9	23.6	804	200	269	183	557	127

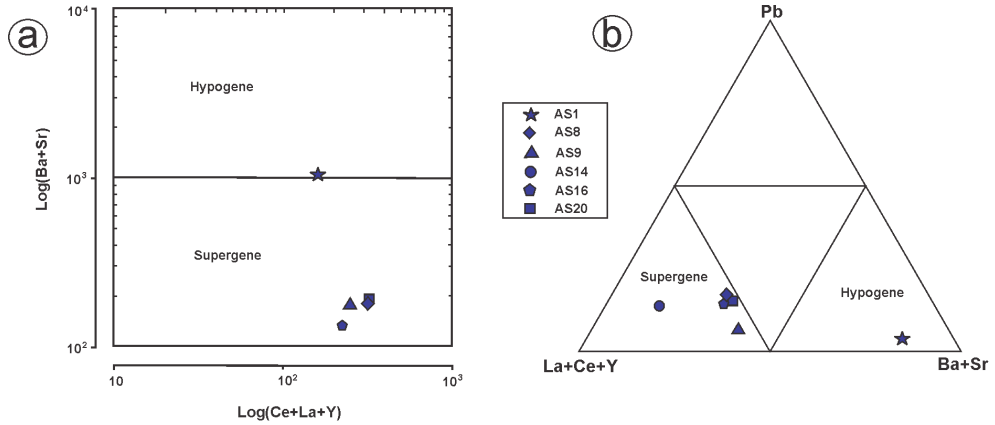

Figure 7. Discrimination diagrams for the supergene–hypogene alteration of the Ropp Complex kaolinites (after [53]). (**a**) The log(Ce+La+Y) vs. log(Ba+Sr) plot; (**b**) The (La+Ce+Y)-(Ba+Sr)-Pb ternary plot.

4.5. Rare Earth Element (REE) Concentration

Large ion lithophile elements (LILEs), such as Sr (40.2–122 ppm), Rb (0.85–674 ppm), Ba (34.6–911 ppm), and Cs (0.071–27.5 ppm) (Table 6), show depletion on the chondrite-normalized spider plot, while high field-strength elements (HFSEs), such as Zr (284–666 ppm), Hf (7.46–57.8 ppm), Nb (18.6–245 ppm), Ta (1.04–40 ppm), and rare earth elements (REE), exhibit relative enrichment. HFSEs are resistant to weathering and are often incorporated in the weathering-resistant accessory minerals (zircon, rutile, and monazite), even after extensive weathering. As such, their concentrations are not expected to be affected.

Table 6. Rare earth element concentrations of whole-rock clays (AS) and the relative bedrocks (AY) (ppm).

Samples	AS1	AS8	AS9	AS14	AS16	AS20	AY3	AY4	AY6	AY8	AY10	AY14
Rock type	**RBG**	**BGM**	**CAB**	**BGM**	**BST**	**CAB**	**RBG**	**RBG**	**ABG**	**BGM**	**BGU**	**CAB**
La	44.6	68.2	67.1	141	62.7	93.4	41.4	85.9	122	9.9	80.0	19.2
Ce	80	143	149	178	134	185	90.9	159	157	24.6	149	42.7
Pr	10.2	14.7	16.4	26.8	14.5	22.5	11.8	17.2	33.0	3.2	20.4	5.5
Nd	37.9	52.4	59.4	77.2	49.3	79.7	36.1	58.5	128	13.9	72.1	22.0
Sm	8.5	9.7	10.9	11.1	8.1	12.0	9.6	9.4	29.4	4.3	17.9	4.9
Eu	1.7	1.6	1.8	1.2	1.6	2.4	0.1	1.2	1.5	1.1	0.5	1.3
Gd	7.8	10.4	8.8	8.7	6.6	7.5	8.8	6.7	27.0	4.4	17.8	4.4
Tb	1.3	1.8	1.4	1.5	1.1	1.0	2.0	0.9	4.0	0.8	3.7	0.7
Dy	6.6	11.7	7.8	9.5	6.3	4.7	13.7	4.8	23.0	5.4	25.4	4.1
Ho	1.2	2.5	1.5	2.0	1.2	0.8	3.0	0.9	4.2	1.1	5.3	0.8
Er	3.1	7.5	3.8	6.5	3.4	2.2	10.4	2.3	11.4	3.2	16.7	2.3
Tm	0.4	1.2	0.6	1.2	0.5	0.3	2.0	0.3	1.6	0.5	2.8	0.3
Yb	2.6	8.8	3.7	9.6	3.5	2.2	15.3	1.9	10.2	3.3	18.9	2.2
Lu	0.4	1.3	0.5	1.4	0.5	0.4	2.2	0.3	1.4	0.5	2.6	0.3

The multi-element diagram (Figure 8a) depicts the depletion of mobile HFSEs (K, Sr, and Ba) and the enrichment of less mobile HFSEs (Th, Ta, and Hf). Europium (Eu) exhibits a very strong negative anomaly (Figure 8b). In general, the parent rock samples exhibit a much more pronounced negative Eu anomaly in comparison to the kaolin-ore samples. The chondrite-normalized REE diagram reveals a depletion of LREEs over HREEs, which is typical for most felsic rocks. The crystal structure of kaolinite exhibits a stronger affinity for LREEs over HREEs and thus leads to a pronounced depletion of Eu. Ce was observed to be more than 100 ppm in the REE compositions of the kaolin-ore samples. La, Nd, and Y were greater than 25 ppm. Other REEs were less than 2 ppm (Eu, Tb, Tm, and Lu), while Sm, Dy, and Gd were usually less than 12 ppm.

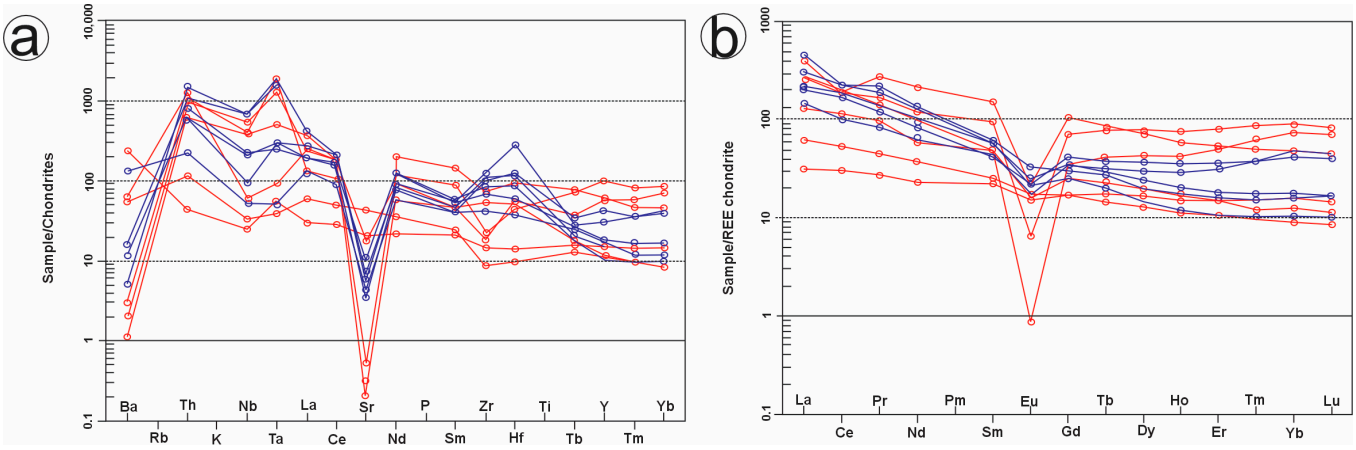

Figure 8. (**a**) Chondrite-normalized trace element diagram (after [54]); (**b**) Chondrite-normalized REE diagram (after [55]). Kaolin-ore samples in blue and bedrock samples in red.

5. Discussion

5.1. Alteration and Element Behavior during Kaolinization

The relatively high Fe_2O_3 averages (3.20%) result from the intense oxidation of iron-bearing silicate minerals, such as biotite, present in the parent rock leading to the formation of more stable iron oxides [56]. The decrease in silica content from the parent rock to the weathered material is due to the transformation of feldspars into kaolinite through weathering processes [57]. CIW (96.82–99.83) and CIA (81.96–99.77) values of the Ropp

Complex kaolinites suggest an extent of alteration processes in the kaolin deposits [33,34]. This indicates that the bedrock from which the kaolin deposits were formed has undergone an extensive breakdown and alteration of their original mineral composition. Furthermore, the low ICV values suggest that the samples are likely derived from a homogeneous parent rock, while the only sample (AS1) with a high ICV originates from the similar bedrock type of riebeckite–biotite granite but experiences a different process of hypogene alteration (Figure 6). Therefore, the high estimated CIA and CIW values and the low ICV values of the kaolin samples suggest the significant weathering of the parent rocks under warm and humid climatic conditions [4–6,21].

The supergene kaolinization process often concentrates HFSEs in a kaolin deposit while depleting mobile LILEs significantly [58,59]. During the kaolinization process, the alteration of feldspars releases Ca, Na, K, and Ba into the altering solutions [58,60]. The decrease in CaO, Na_2O, and K_2O in the study area could be influenced by feldspar weathering, while the decrease in MgO and Fe_2O_3 could be due to the breakdown of biotite alongside the feldspars. These extremely mobile components can be rapidly leached out of the system during weathering processes. The relative enrichment in TiO_2 and Al_2O_3 could be a result of the formation of secondary mineral phases, particularly rutile and clay minerals [4]. The resembling pattern of HFSEs and LILEs between the kaolins in the study area reflects the intensity of weathering. During the weathering process, REEs and HFSEs remain immobile [61]. As a result of the aforementioned process, it can be inferred that weathering processes during kaolinization of the deposit concentrate HFSEs and deplete LILEs in the kaolin-ore sample. The depletion in LILEs (Rb, Ba, and Sr) and the enrichment in HFSEs (Zr, Nb, and Hf) indicate that the source rock of the kaolin deposits has a felsic composition [62]. The presence of a large amount of illite suggests that the kaolin deposit (AS1) has experienced hydrothermal alteration in the burial stage due to the heating of groundwater by the late volcanism instead of surface chemical weathering. The initial alteration of igneous rocks usually produces smectite, which transforms rapidly to kaolinite, with weathering proceeding under tropical to subtropical climate conditions [58,59], as also indicated by the discrimination diagram for the supergene–hypogene alteration of kaolins (Figure 7). The loss of Na, K, and Ca can be explained by their significant mobility during weathering [63].

The weathering processes and the characteristics of the parent rock affect how trace elements are distributed in clays in sediments and soils [4–6,62,64–66]. In comparison with the parent rocks, the Ropp Complex kaolinite samples are depleted in Rb, Sr, and Ba and enriched in Zr, Cr, Ni, Cu, and Zn. The zirconium content of the kaolins is relatively high, and such a high Zr content suggests that the parent rock contained zirconium-rich minerals in significant amounts. Zirconium minerals, like zircon, have relatively high concentrations of zirconium compared to other common rock-forming minerals.

The Ropp Complex kaolinite samples are more Ba enriched (mean 225.83 ppm) than Sr enriched (mean 70.23 ppm). The relative abundance of feldspars in the parent rock and their stability contribute a substantial role in the enrichment of barium compared to strontium in the kaolin samples [67]. The values of Cr and Ni in kaolin can provide evidence to differentiate a felsic (silica-rich) source from a mafic (magnesium- and iron-rich) source. A low Cr (<100 ppm) and nickel (<50 ppm) content suggests a felsic origin, as it represents the absorption of small Cr and Ni ions to clay particles during the weathering of rocks containing Cr- and Ni-bearing minerals. High concentrations of Cr and Ni, on the other hand, are generally observed in sediments originating from ultramafic rocks [68]. The contents of Cr (mean 92.88 ppm) and Ni (mean 25.1 ppm) are low in the Ropp Complex kaolins, consistent with their felsic parent rocks. Nb and V exhibit lower mobility, aligning with established knowledge regarding their behavior during the process of weathering [69]. Great values of V, Cr, and Cu in the kaolin samples indicate the influence of chromophore elements on variations in the color of the kaolins.

REE geochemistry can provide useful evidence for a source of kaolin deposits [70,71]. The absence of a Ce anomaly and negative Eu anomaly are considered a result of feldspar

alteration and the formation of clay minerals under elevated temperatures [72]. The Ropp Complex kaolin deposits show a higher concentration of LREEs relative to HREEs and display a distinct negative Eu anomaly while lacking Ce anomalies, suggesting a supergene origin. The magnitude of the negative Eu anomaly differs between the host rocks and the kaolins, with stronger anomalies observed in the rocks than in the kaolins. This variation in the extent of negative Eu anomalies may be linked to differences in the compositions of the source rocks. Our findings are consistent with the work of Odewumi et al. (2015) [20]. However, chemical weathering typically has a limited effect on the distribution pattern of rare earth elements in weathered profiles [73,74].

5.2. Genesis of the Kaolin Deposit

Kaolin deposits can be classified as hypogene (hydrothermal) or supergene (weathering) depending on the kaolinization process of the parent rock. Hypogene kaolins form in hydrothermal systems where hot, element-rich fluids circulate through the parent rock [75–78]. Hydrothermal kaolin deposits are commonly linked with high-temperature alteration minerals, including pyrophyllite, diaspore, nacrite, dickite, and topaz [53,79]. On the other hand, illite usually forms from the alteration of muscovite and feldspar in potassium-rich environments and is often associated with hydrothermal processes, particularly in low-temperature environments compared to the high-temperature minerals mentioned above [80,81]. It is also considered a significant mineral in supergene environments due to physical weathering under cold and arid climates [82]. However, under the warm and humid climate conditions in the area, the association of illite with kaolinite in the Ropp Complex kaolin (AS1) may indicate a complex alteration history involving both hydrothermal activity and supergene weathering processes [80], taking into account the presence of almost no illite observed in the weathering regolith of other locations around the area (Figure 6). In the triangular ACNK diagram, most of the kaolin samples fall close to the Al_2O_3 peak position, and the geochemical evolution trend clearly indicates a genetic relationship of intense weathering between the kaolin deposit and the granite bedrock (e.g., [42]). Obviously, the source of the kaolin deposits is presumed to be the biotite granite. This is also supported by field investigations, which revealed that numerous kaolin occurrences were connected with the granite bedrock. In addition, the notably high kaolinite content in kaolin-ore samples suggests an intense chemical leaching during the weathering process. It can also be inferred from the ACNK diagram that the kaolin was formed under a warm and humid climate with efficient drainage, as illustrated in Figure 9.

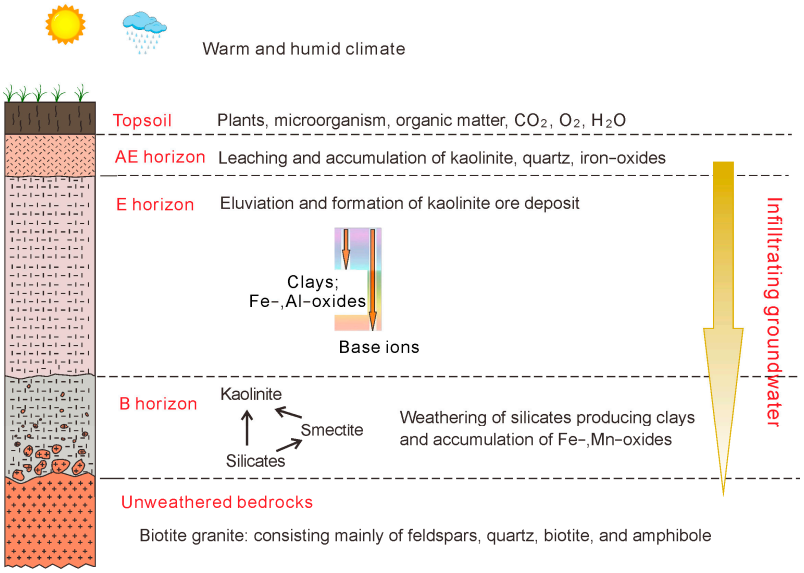

Figure 9. A proposed model of formation of the Ropp Complex kaolins.

LILEs are mostly concentrated by hydrothermal alteration, and a common kaolin deposit formed through hydrothermal fluid exhibits a silica/alumina ratio ranging from 1.04 to 1.45 [58,83]. Kaolin can also develop through diagenetic processes within sedimentary basins [84]. The kaolin deposits in the study area show a SiO_2/Al_2O_3 content range between 1.32 and 2.27, and this range is characteristic of a mixed origin. Binary and ternary plots of different major and trace element combinations have been used to identify the formation of hypogene and supergene kaolin formations. In almost all cases, the samples from the study area were plotted mainly within the supergene field, while sample AS1 shows some affinity to the hypogene field, as confirmed by the chemical alteration index (Figure 7). All these lend credence to the clay deposits' supergene origin, with little impact of the hypogene origin, and also indicate intensive weathering. Furthermore, the LOI of the kaolin deposits ranges from 7.02 to 16.73% (average 12.24%), comparable to the well-known deposits in Georgia (13%) and Cornwall (13.6%) [40].

5.3. Grade, Quality, and Economic Significance

Except for the AS1 kaolin, in which kaolinite occurs as a minor phase (20%), all other Ropp Complex kaolins contain a markedly high amount of kaolinite, up to 77%–98% (Table 1). The kaolinite content significantly influences the kaolin grade [40]. High-grade deposits contain over 75% kaolinite [85]. Obviously, kaolin deposits in the Ropp Complex meet the high-grade criterion.

The quality of kaolin is dependent on the type and quantity of impurities present. Impurities are often observed adhering to the kaolinite surface or substituting a component inside the kaolinite crystal structure [40]. Kaolins containing Fe and Ti are crucial in identifying their quality because they provide the kaolin yellow, pink, or deeper hues [86]. The relatively higher contents of Fe_2O_3 (1.23%–7.54%) and TiO_2 (0.64%–2.75%) as well as the significantly lower crystallinity (HI value of 0.53–1.1) of kaolinite of the Ropp Complex kaolin deposits do not meet the requirement for filler and paper coating industries, unlike those reported by Daspan et al. (2009) [18]. Fe_2O_3 in kaolin typically has a higher tolerance as a supplementary cementitious material (SCM) than other applications, like ceramics and paper.

The economic importance of kaolin deposits is determined by the mineralogical, chemical, and physical properties that govern their applicability [87]. The collected data on the Ropp Complex kaolin deposits indicate that it is well suited for manufacturing porcelain, ceramic tableware, sanitary ware, high-grade refractories, premium ceramic tiles, and specialty paper coating. The chemical constituents SiO_2 (46%) and Al_2O_3 (38%) are the major components of kaolin [88]. Although the kaolinite content is within the range of chemical compositions (81%–93%) necessary for the ceramic industry [37], the concentrations of Fe_2O_3 and TiO_2 require some beneficiations.

Most toxic elements, such as Hg, As, Sb, and Cd, were not detectable due to their low concentration. The low concentration of MgO, CaO, Na_2O, and K_2O in the kaolin deposits make them highly suitable for use in the pharmaceutical and cosmetic industries, and their elevated SiO_2 and Fe_2O_3 levels also make them well suited for filling applications. The crucial requirement for the industrial utilization of kaolin is its chemical composition aligning closely with its theoretical composition. However, achieving this is often challenging due to the association of kaolinite with other minerals and its rarity in a pure form [9].

The grade and applications of the Ropp Complex kaolins are compared to known commercial kaolins from Cornwall deposits, deposits from English China clay (ECC), and Sekeharman kaolin (SKD) [89]. The markedly high grade of kaolinite for the Ropp Complex kaolins makes them potential wide application prospects. The only limitation is the impurities (Fe_2O_3 and TiO_2) in the Ropp Complex kaolinitic clays, which can be removed through beneficiation (Table 4). To generate a good-grade product, Fe_2O_3 can vary from 0.2 to 1.0%, and TiO_2 can range from 1% to 2.2% [90]. The chemical characteristics ($SiO_2 + Al_2O_3 + Fe_2O_3 > 70\%$) and kaolinite content (kaolinite > 65%) of the Ropp Complex kaolins also indicate that they can probably be utilized as a supplementary cementitious

material for the cement industry, which is a potential approach for reducing CO_2 emissions and improving the overall sustainability of the construction sector [91].

6. Conclusions

The mineralogical and geochemical investigation of clay fractions and bulk samples from primary kaolin deposits formed on biotite granites has provided insights into their origin. The pronounced negative Eu anomaly, along with the relative enrichment of LREEs over HREEs, and the absence of a Ce anomaly strongly indicates a supergene origin for the Ropp Complex kaolins. Particularly noteworthy is the enrichment of chemically immobile elements (Al_2O_3, TiO_2, Zr, and Sc), coupled with the depletion of mobile elements (MgO, CaO, Na_2O, and K_2O) and the notably high CIA value (81.96–99.73), indicating the significant chemical weathering of the parent rock. Except for AS1 kaolin with minor kaolinite (20%), all other kaolins dominantly contain kaolinite with a content of 77%–98%. The crystallinity of kaolinite is significantly low, with an HI value ranging from 0.53 to 1.1, consistent with their notably small grain size, indicating that kaolinite formed from the intensive chemical weathering of igneous rocks. The observed chemical correlations in the kaolin samples align with the anticipated mineralogical transformations during supergene weathering and kaolin formation. Exceptionally, the AS1 kaolin with dominantly illite (65%) was probably formed from hydrothermal alteration in the burial stage due to the heating of groundwater by the late volcanism. Furthermore, a comparative analysis of the chemical composition between the Ropp Complex kaolin and a renowned deposit in Cornwall, the UK, underscores the economic potential of the Ropp Complex deposits.

Author Contributions: A.Y.: Writing original draft. H.H.: Review and editing, Supervision, Funding acquisition, and Conceptualization. C.L., Y.X. and X.Z.: Analytical works. A.S. and T.A. partially contributed with idea discussion and manuscript writing. Z.L.: Manuscript editing. All authors have read and agreed to the published version of the manuscript.

Funding: This research was funded by the National Natural Science Foundation of China (Projects 42172045 and 41972040).

Data Availability Statement: All data are available upon request.

Acknowledgments: The authors thank Wang Hongquan and Chen Jin for assistance in sample preparation and SEM analysis; they are also grateful to the anonymous reviewers for their insightful reviews, valuable comments, and constructive suggestions.

Conflicts of Interest: The authors declare that they have no competing financial interests or personal relationships that could have appeared to influence the work reported in this paper.

References

1. Christidis, G.E. Assessment of Industrial Clays. In *Developments in Clay Science*; Elsevier: Amsterdam, The Netherlands, 2013; Volume 5, pp. 425–449. [CrossRef]
2. Harvey, C.C.; Murray, H.H. Industrial clays in the 21st century: A perspective of exploration, technology and utilization. *Appl. Clay Sci.* **1997**, *11*, 285–310. [CrossRef]
3. Murray, H.H. Traditional and new applications for kaolin, smectite, and palygorskite: A general overview. *Appl. Clay Sci.* **2000**, *17*, 207–221. [CrossRef]
4. Dill, H.G. Kaolin: Soil, rock and ore: From the mineral to the magmatic, sedimentary and metamorphic environments. *Earth-Sci. Rev.* **2016**, *161*, 16–129. [CrossRef]
5. Tangari, A.C.; Scarciglia, F.; Piluso, E.; Marinangeli, L.; Pompilio, L. Role of weathering of pillow basalt, pyroclastic input and geomorphic processes on the genesis of the Monte Cerviero upland soils (Calabria, Italy). *CATENA* **2018**, *171*, 299–315. [CrossRef]
6. Tangari, A.C.; Le Pera, E.; Andò, S.; Garzanti, E.; Piluso, E.; Marinangeli, L.; Scarciglia, F. Soil-formation in the central Mediterranean: Insight from heavy minerals. *CATENA* **2021**, *197*, 104998. [CrossRef]
7. Guggenheim, S.; Adams, J.M.; Bain, D.C.; Bergaya, F.; Brigatti, M.F.; Drits, V.A.; Formoso, M.L.L.; Galán, E.; Kogure, T.; Stanjek, H. Summary of recommendations of Nomenclature Committees relevant to clay mineralogy: Report of the association Internationale pour l'Etude des Argiles (AIPEA) Nomenclature Committee for 2006. *Clays Clay Miner.* **2006**, *54*, 761–772. [CrossRef]
8. Murray, H.H. Clays. In *Ullmann's Encyclopedia of Industrial Chemistry*, 1st ed.; Wiley-VCH: Weinheim, Germany, 2007. [CrossRef]
9. Ekosse, G.-I.E. Kaolin deposits and occurrences in Africa: Geology, mineralogy and utilization. *Appl. Clay Sci.* **2010**, *50*, 212–236. [CrossRef]

10. Murray, H.H. Chapter 3 Geology and Location of Major Industrial Clay Deposits. In *Developments in Clay Science*; Murray, H.H., Ed.; Applied Clay Mineralogy; Elsevier: Amsterdam, The Netherlands, 2006; Volume 2, pp. 33–65. [CrossRef]
11. Awad, M.; Galindo, A.; Setti, M.; El-Rahmany, M.; Viseras, C. Kaolinite in pharmaceutics and biomedicine. *Int. J. Pharm.* **2017**, *533*, 34–48. [CrossRef]
12. Onyemaobi, O.O.; Nekede, F.P.; Mark, U. Mineral Resources Exploitation, Processing and Utilization-A Sine Qua Non for Nigeria's Metallurgical Industrial Development. *Inaug. Lect. Ser.* **2002**, *5*, 48.
13. Oyebanjo, O.M.; Ekosse, G.E.; Odiyo, J.O. Mineral Constituents and Kaolinite Crystallinity of the < 2 µm Fraction of Cretaceous-Paleogene/Neogene Kaolins from Eastern Dahomey and Niger Delta Basins, Nigeria. *Open Geosci.* **2018**, *10*, 157–166. [CrossRef]
14. Akinyele, J.O.; Odunfa, S.O.; Famoye, A.A.; Kuye, S.I. Structural behaviour of metakaolin infused concrete structure. *Niger. J. Technol.* **2017**, *36*, 331–338. [CrossRef]
15. Adeniyi, A.G.; Abdulkareem, S.A.; Emenike, E.C.; Abdulkareem, M.T.; Iwuozor, K.O.; Amoloye, M.A.; Ahmed, I.I.; Awokunle, O.E. Development and characterization of microstructural and mechanical properties of hybrid polystyrene composites filled with kaolin and expanded polyethylene powder. *Results Eng.* **2022**, *14*, 100423. [CrossRef]
16. Adeniyi, A.G.; Iwuozor, K.O.; Emenike, E.C. Material Development Potential of Nigeria's Kaolin. *Chem. Afr.* **2023**, *6*, 1709–1725. [CrossRef]
17. Fang, Q.; Hong, H.; Zhao, L.; Furnes, H.; Lu, H.; Han, W.; Liu, Y.; Jia, Z.; Wang, C.; Yin, K.; et al. Tectonic uplift-influenced monsoonal changes promoted hominin occupation of the Luonan Basin: Insights from a loess-paleosol sequence, eastern Qinling Mountains, central China. *Quat. Sci. Rev.* **2017**, *169*, 312–329. [CrossRef]
18. Daspan, R.I.; Yakubu, J.A.; Taiwo, A.O. A preliminary chemical and physical assessment of the kuba kaolin deposit, Jos Plateau (North-Central Nigera). *Cont. J. Earth Sci.* **2009**, *4*, 1–11.
19. Christopher, O.S.; Johnson, O.O.; Bernard, G.R. Mineralogy and pedogenesis of Kuba clays within Ropp Complex, Jos Plateau, Northcentral Nigeria. *Int. J. Earth Sci. Eng.* **2013**, *6*, 434–441.
20. Odewumi, S.C.; Adekeye, J.I.D.; Ojo, O.J. Trace and rare earth elements geochemistry of Kuba (Major porter) and Nahuta clays, Jos Plateau, northcentral Nigeria: Implications for provenance. *J. Min. Geol.* **2015**, *50*, 71–82.
21. Odewumi, S.C. Major and Trace Elements Geochemical Characteristics of Nahuta Clay, Jos Plateau, Northcentral Nigeria: Implications for Paleoweathering Proxy. *NSUK J. Sci. Technol. NJST* **2020**, *7*, 71–76.
22. Oyawoye, M.O.; Hirst, D.M. Occurrence of a montmorillonite mineral in the Nigerian younger granites at Ropp, Plateau Province, Northern Nigeria. *Clay Miner. Bull.* **1964**, *5*, 427–433. [CrossRef]
23. Cravero, F.; Gonzalez, I.; Galan, E.; Dominguez, E. Geology, mineralogy, origin and possible applications of some Argentinian kaolins in the Neuquen basin. *Appl. Clay Sci.* **1997**, *12*, 27–42. [CrossRef]
24. Buchannan, M.S.; Macleod, W.N.; Turner, D.C. The geology of the Jos Plateau. *Geol. Surv. Niger. Bull.* **1971**, *32*, 107–119.
25. Pastor, J.; Turaki, U.M. Primary mineralization in Nigerian ring complexes and its economic significance. *J. Afr. Earth Sci. (1983)* **1985**, *3*, 223–227. [CrossRef]
26. Kamaunji, V.; Wang, L.-X.; Bala Girei, M.; Zhu, Y.-X.; Li, L.; Vincent, V.; Amuda, A. Petrogenesis and tectonic implication of the alkaline ferroan granites from Ropp complex, north-central Nigeria: Clues from zircon chemistry, U–Pb dating, and Lu–Hf isotope. *Geol. J.* **2022**, *58*, 21–50. [CrossRef]
27. Olasehinde, A.; Ashano, E.; Singh, G. Structural Analysis the Ropp Complex, North Central Nigeria, using Magnetic Anomaly and Landsat Etm Imagery. *Cont. J. Earth Sci* **2012**, *7*, 1–8.
28. Amuda, A.; Yang, X.; Deng, J.; Faisal, M.; Cao, J.; Ibrahim Bute, S.; Bala Girei, M.; Elatikpo, M. Petrogenesis of the peralkaline Dutsen Wai and Ropp complexes in the Nigerian younger granites: Implications for crucial metal enrichments. *Int. Geol. Rev.* **2020**, *63*, 2057–2081. [CrossRef]
29. Jacobson, R.R.E.; Macleod, W.N.; Black, R. Ring-complexes in the younger granite province of northern Nigeria. *Geol. Soc. Lond. Mem.* **1958**, *1*, 78.
30. Srodon, J. Identification and quantitative analysis of clay minerals. *Handb. Clay Sci.* **2006**, *1*, 765–787.
31. Hillier, S. Accurate quantitative analysis of clay and other minerals in sandstones by XRD: Comparison of a Rietveld and a reference intensity ratio (RIR) method and the importance of sample preparation. *Clay Miner.* **2000**, *35*, 291–302. [CrossRef]
32. Hinckley, D.N. Variability in 'crystallinity' values among the kaolin deposits of the coastal plain of Georgia and South Carolina. *Clays Clay Miner.* **1962**, *11*, 229–235. [CrossRef]
33. Harnois, L. The CIW index: A new chemical index of weathering. *Sediment. Geol.* **1988**, *55*, 319–322. [CrossRef]
34. Nesbitt, H.W.; Young, G.M. Early Proterozoic climates and plate motions inferred from major element chemistry of lutites. *Nature* **1982**, *299*, 715–717. [CrossRef]
35. Cox, R.; Lowe, D.R.; Cullers, R. The influence of sediment recycling and basement composition on evolution of mudrock chemistry in the southwestern United States. *Geochim. Cosmochim. Acta* **1995**, *59*, 2919–2940. [CrossRef]
36. Hong, H.; Wang, J.; Wang, C.; Liu, C.; Algeo, T.J.; Zhao, L.; Zhou, L.; Zhang, D.; Fang, Q. Clay and Fe (oxyhydr)oxide mineralogy in the basalt weathering profile in Hainan (southern China): Implications for pedogenesis process. *Clays Clay Miner.* **2024**, *72*, e8. [CrossRef]
37. Bloodworth, A.J.; Highley, D.E.; Mitchell, C.J. Industrial minerals laboratory manual: Kao-lin. *Br. Geol. Surv. Tech. Rep.* **1993**, *1*, WG/93/1.
38. Jepson, W.B. Kaolins: Their properties and uses. *Philos. Trans. R. Soc. London. Ser. A Math. Phys. Sci.* **1984**, *311*, 411–432. [CrossRef]

39. Nesbitt, H.W.; Young, G.M.; McLennan, S.M.; Keays, R.R. Effects of Chemical Weathering and Sorting on the Petrogenesis of Siliciclastic Sediments, with Implications for Provenance Studies. *J. Geol.* **1996**, *104*, 525–542. [CrossRef]
40. Ekosse, G. Provenance of the Kgwakgwe kaolin deposit in Southeastern Botswana and its possible utilization. *Appl. Clay Sci.* **2001**, *20*, 137–152. [CrossRef]
41. Highley, D.E. China Clay. *Br. Geol. Surv. Lond.* **1984**, *26*, NT26.
42. Shao, J.; Yang, S.; Li, C. Chemical indices (CIA and WIP) as proxies for integrated chemical weathering in China: Inferences from analysis of fluvial sediments. *Sediment. Geol.* **2012**, *265-266*, 110–120. [CrossRef]
43. Bukalo, N.N.; Ekosse, G.-I.E.; Odiyo, J.O.; Ogola, J.S. Geochemistry of Selected Kaolins from Cameroon and Nigeria. *Open Geosci.* **2017**, *9*, 600–612. [CrossRef]
44. Nesbitt, H.; Young, G. Prediction of some weathering trends of plutonic and volcanic rocks based on thermodynamic and kinetic considerations. *Geochim. Cosmochim. Acta* **1984**, *48*, 1523–1534. [CrossRef]
45. Nesbitt, H.W.; Young, G.M. Formation and Diagenesis of Weathering Profiles. *J. Geol.* **1989**, *97*, 129–147. [CrossRef]
46. Nesbitt, H.W.; Young, G.M. Petrogenesis of sediments in the absence of chemical weathering: Effects of abrasion and sorting on bulk composition and mineralogy. *Sedimentology* **1996**, *43*, 341–358. [CrossRef]
47. Annon Kaolin in the UK, English China clay deposits on its lead-in world paper. *Indones. Min.* **1972**, *52*, 9–29.
48. Singer, F.; Sonja, S.S. *Industrial Ceramics*; Chapman and Hall: London, UK, 1971.
49. Parker, E.R. For Engineers and Scientists. In *Material Data Book*; McGraw Hill: New York, NY, USA, 1967.
50. Harben, P.W. *The Industrial Minerals Handybook: A Guide to Markets, Specifications, & Prices*, 3rd ed.; Industrial Minerals Information, Ltd.: Surrey, UK, 1999.
51. Lopezgalindo, A.; Viseras, C.; Cerezo, P. Compositional, technical and safety specifications of clays to be used as pharmaceutical and cosmetic products. *Appl. Clay Sci.* **2007**, *36*, 51–63. [CrossRef]
52. RMRDC. *Raw Materials Research and Development Council (RMRDC) Multidisciplinary Committee Techno-Economic Survey (MCTS)Report*; Chemicals and Pharmaceutical Sector: Abuja, Nigeria, 2003; pp. 16–69.
53. Dill, H.G.; Bosse, H.-R.; Henning, K.-H.; Fricke, A.; Ahrendt, H. Mineralogical and chemical variations in hypogene and supergene kaolin deposits in a mobile fold belt the Central Andes of northwestern Peru. *Miner. Depos.* **1997**, *32*, 149–163. [CrossRef]
54. Thompson, R.N. Magmatism of the British Tertiary Volcanic Province. *Scott. J. Geol.* **1982**, *18*, 49–107. [CrossRef]
55. Boynton, W.V. Chapter 3—Cosmochemistry of the Rare Earth Elements: Meteorite Studies. In *Developments in Geochemistry*; Henderson, P., Ed.; Rare Earth Element Geochemistry; Elsevier: Amsterdam, The Netherlands, 1984; Volume 2, pp. 63–114.
56. Ariffin, K.S.; Rahman, H.A.; Hussin, H.; Hadi, K.A.A. The genesis and characteristics of primary kaolinitic clay occurrence at Bukit Lampas, Simpang Pulai, Ipoh. *Bull. Geol. Soc. Malays.* **2008**, *54*, 9–16. [CrossRef]
57. Karadağ, M.M.; Küpeli, Ş.; Arýk, F.; Ayhan, A.; Zedef, V.; Döyen, A. Rare earth element (REE) geochemistry and genetic implications of the Mortaş bauxite deposit (Seydişehir/Konya–Southern Turkey). *Geochemistry* **2009**, *69*, 143–159. [CrossRef]
58. Abedini, A.; Calagari, A.A. Geochemical characteristics of the Abgarm kaolin deposit, NW Iran. *Neues Jahrb. Fur Geol. Und Palaontol.-Abh.* **2015**, *278*, 335–350. [CrossRef]
59. Fernández-Caliani, J.; Galán, E.; Aparicio, P.; Miras, A.; Márquez, M. Origin and geochemical evolution of the Nuevo Montecastelo kaolin deposit (Galicia, NW Spain). *Appl. Clay Sci.* **2010**, *49*, 91–97. [CrossRef]
60. McLennan, S.M.; Taylor, S.R. Sedimentary Rocks and Crustal Evolution: Tectonic Setting and Secular Trends. *J. Geol.* **1991**, *99*, 1–21. [CrossRef]
61. Jiang, S.-Y.; Wang, R.-C.; Xu, X.-S.; Zhao, K.-D. Mobility of high field strength elements (HFSE) in magmatic-, metamorphic-, and submarine-hydrothermal systems. *Phys. Chem. Earth Parts A/B/C* **2005**, *30*, 1020–1029. [CrossRef]
62. Taylor, S.R.; McLennan, S.M. *The Continental Crust: Its Composition and Evolution*, 1st ed.; Blackwell: Oxford, UK, 1985.
63. Cullers, R. Mineralogical and chemical changes of soil and stream sediment formed by intense weathering of the Danburg granite, Georgia, U.S.A. *Lithos* **1988**, *21*, 301–314. [CrossRef]
64. Garrels, R.M.; Mackenzie, F.T. *Evolution of Sedimentary Rocks*; Norton: Tempe, AZ, USA, 1971.
65. Nesbitt, H.; Markovics, G.; Price, R. Chemical processes affecting alkalis and alkaline earths during continental weathering. *Geochim. Cosmochim. Acta* **1980**, *44*, 1659–1666. [CrossRef]
66. Wronkiewicz, D.J.; Condie, K.C. Geochemistry of Archean shales from the Witwatersrand Supergroup, South Africa: Source-area weathering and provenance. *Geochim. Cosmochim. Acta* **1987**, *51*, 2401–2416. [CrossRef]
67. Puchelt, H. Barium: Behavior during processes connected with magmatism. In *Handbook of Geochemistry*; Springer: Berlin/Heidelberg, Germany, 1972.
68. Patterson, S.H.; Murray, H.H. Kaolin, refractory clay, ball clay, and halloysite in North America, Hawaii, and the Caribbean region. *Prof. Pap.* **1984**, 1306. [CrossRef]
69. Middelburg, J.J.; van der Weijden, C.H.; Woittiez, J.R. Chemical processes affecting the mobility of major, minor and trace elements during weathering of granitic rocks. *Chem. Geol.* **1988**, *68*, 253–273. [CrossRef]
70. Prudêncio, M.I.; Gouveia, M.A.; Braga, M.A.S. *REE* distribution in presentday and ancient surface environments of basaltic rocks (Central Portugal). *Clay Miner.* **1995**, *30*, 239–248. [CrossRef]
71. Santos, I.R.; Fávaro, D.I.; Schaefer, C.E.; Silva-Filho, E.V. Sediment geochemistry in coastal maritime Antarctica (Admiralty Bay, King George Island): Evidence from rare earths and other elements. *Mar. Chem.* **2007**, *107*, 464–474. [CrossRef]

72. Lackschewitz, K.S.; Singer, A.; Botz, R.; Garbe-Schonberg, D.; Stoffers, P.; Horz, K. Formation and Transformation of Clay Minerals in the Hydrothermal Deposits of Middle Valley, Juan de Fuca Ridge, ODP Leg 169. *Econ. Geol.* **2000**, *95*, 361–389. [CrossRef]
73. Galán, E.; Aparicio, P.; Fernández-Caliani, J.C.; Miras, A.; Márquez, M.G.; Fallick, A.E.; Clauer, N. New insights on mineralogy and genesis of kaolin deposits: The Burela kaolin deposit (Northwestern Spain). *Appl. Clay Sci.* **2016**, *131*, 14–26. [CrossRef]
74. Hong, H.; Fang, Q.; Cheng, L.; Wang, C.; Churchman, G.J. Microorganism-induced weathering of clay minerals in a hydromorphic soil. *Geochim. Cosmochim. Acta* **2016**, *184*, 272–288. [CrossRef]
75. Baioumy, H.M.; Ismael, I.S. Composition, origin and industrial suitability of the Aswan ball clays, Egypt. *Appl. Clay Sci.* **2014**, *102*, 202–212. [CrossRef]
76. Gilg, H.A.; Hülmeyer, S.; Miller, H.; Sheppard, S.M.F. Supergene Origin of the Lastarria Kaolin Deposit, South-Central Chile, and Paleoclimatic Implications. *Clays Clay Miner.* **1999**, *47*, 201–211. [CrossRef]
77. Murray, H.H. World kaolins—diverse quality needs permit different resource types. In Proceedings of the US Minerals International. Congress, Las Vegas, NV, USA; 1988; pp. 127–130.
78. Murray, H.H.; Keller, W.D. Kaolins, Kaolins, and Kaolins. In *Kaolin Genesis and Utilization*; Murray, H.H., Bundy, W.M., Harvey, C.C., Eds.; Clay Minerals Society: Chantilly, VA, USA, 1993; Volume 1.
79. Arribas, A.; Hedenquist, J.; Itaya, T.; Okada, T.; Concepción, R.; Garcia, J.S., Jr. Contemporaneous formation of adjacent porphyry and epithermal Cu-Au deposits over 300 ka in northern Luzon, Philippines. *Geology* **1995**, *23*, 337–340. [CrossRef]
80. Deon, F.; van Ruitenbeek, F.; van der Werff, H.; van der Meijde, M.; Marcatelli, C. Detection of Interlayered Illite/Smectite Clay Minerals with XRD, SEM Analyses and Reflectance Spectroscopy. *Sensors* **2022**, *22*, 3602. [CrossRef]
81. Ece, I.; Ercan, H. Global Occurrence, Geology and Characteristics of Hydrothermal-Origin Kaolin Deposits. *Minerals* **2024**, *14*, 353. [CrossRef]
82. Papoulis, D. Supergene jarosite formation within smectite and illite hydrothermal zones from Limnos Island, Northeast Aegean sea, Greece. *Int. Multidiscip. Sci. GeoConference SGEM* **2008**, *1*, 299–306.
83. Giese, R.F.J. Chapter 3. Kaolin Minerals: Structures and Stabilities. In *Hydrous Phyllosilicates*; De Gruyter: Berlin, Germany, 1988; pp. 29–66, ISBN 978-1-5015-0899-8.
84. Galán, E.; Ferrell, R. Genesis of Clay Minerals. *Dev. Clay Sci.* **2013**, *5*, 83–126. [CrossRef]
85. Awad, M.E.; López-Galindo, A.; Sánchez-Espejo, R.; Sainz-Díaz, C.I.; El-Rahmany, M.M.; Viseras, C. Crystallite size as a function of kaolinite structural order-disorder and kaolin chemical variability: Sedimentological implication. *Appl. Clay Sci.* **2018**, *162*, 261–267. [CrossRef]
86. Kulkarni, M.M.; Jadhav, G.N. Reduction of titaniferrous impurities from kaolin by selective adsorption of flocculating agents. *Int. J. Sci. Eng. Res.* **2016**, *7*, 2229–5518.
87. Prasad, M.; Reid, K.; Murray, H. Kaolin: Processing, properties and applications. *Appl. Clay Sci.* **1991**, *6*, 87–119. [CrossRef]
88. Detlef, G. 2. Mineralogie. In *Füllstoffe*; Vincentz Network: Hannover, Germany, 2019; pp. 17–40. [CrossRef]
89. Konta, J. Clay and man: Clay raw materials in the service of man. *Appl. Clay Sci.* **1995**, *10*, 275–335. [CrossRef]
90. Murray, H.H. Overview—clay mineral applications. *Appl. Clay Sci.* **1991**, *5*, 379–395. [CrossRef]
91. Zunino, F.; Boehm-Courjault, E.; Scrivener, K. The impact of calcite impurities in clays containing kaolinite on their reactivity in cement after calcination. *Mater. Struct.* **2020**, *53*, 44. [CrossRef]